

**Nanoindentation of single- (Fe) and dual-beam (Fe and He) ion-irradiated  
ODS Fe-14Cr-based alloys: Effect of the initial microstructure on  
irradiation-induced hardening**

Heintze, C.; Hilger, I.; Bergner, F.; Weissgärber, T.; Kieback, B.;

Originally published:

March 2019

**Journal of Nuclear Materials 518(2019), 1-10**

DOI: <https://doi.org/10.1016/j.jnucmat.2019.02.037>

Perma-Link to Publication Repository of HZDR:

<https://www.hzdr.de/publications/Publ-28308>

Release of the secondary publication  
on the basis of the German Copyright Law § 38 Section 4.

CC BY-NC-ND

# **Nanoindentation of single- and dual-beam (Fe and He) ion-irradiated ODS Fe-14Cr-based alloys: Effect of the initial microstructure**

C. Heintze<sup>1</sup>, I. Hilger<sup>1,2</sup>, F. Bergner<sup>1\*</sup>, T. Weissgärber<sup>3</sup>, B. Kieback<sup>3</sup>

<sup>1</sup> Helmholtz-Zentrum Dresden – Rossendorf, Institute of Resource Ecology, Bautzner Landstr. 400, 01328 Dresden, Germany

<sup>2</sup> Technische Universität Dresden, Institut für Werkstoffwissenschaft, 01062 Dresden, Germany

<sup>3</sup> Fraunhofer Institute for Manufacturing Technology and Advanced Materials, Branch Lab Dresden, 01277 Dresden, Germany

## **Abstract**

Although the view that nm-sized oxide particles modify and essentially improve the irradiation resistance of Fe-Cr-based alloys is widely accepted, the correctness of this view has only been demonstrated in singular cases. An extension of the field of considered microstructures, irradiation conditions, and measures of irradiation resistance is required. The present study is focused on nanostructured ferritic Fe-14%Cr-based alloys, with and without the addition of 0.6 wt% Y<sub>2</sub>O<sub>3</sub>, produced via mechanical alloying and consolidation by spark plasma sintering. The materials were exposed to single-beam (Fe) and dual-beam (Fe+He) ion irradiations at room temperature. The initial microstructures were characterized, bimodal grain size distributions were observed and nanoindentation was applied to measure irradiation hardening for fine-grained and coarse-grained areas separately. We have found that grain size governs irradiation hardening for single-beam irradiation, while oxide nanoparticles play a dominant role for dual-beam irradiations. This sheds a light on the role of particle-matrix interfaces on helium management.

**Keywords:** Nanostructured ferritic alloys, oxide dispersion strengthening, ion irradiation, dual-beam irradiation, helium, nanoindentation, irradiation hardening

## **1. Introduction**

Advanced oxide-dispersion strengthened (ODS) Fe-xCr-based alloys ( $x > 12\%$ ), also referred to as nanostructured ferritic alloys (NFA), are candidate materials for fission [1] and fusion [2] applications. While the basic understanding on microstructures and mechanical properties is well advanced, the scale up from lab-scale to industrial-scale production of NFAs is still in progress [3]. A typical

---

\* Corresponding author, e-mail f.bergner@hzdr.de

fabrication route to NFA is based on mechanical alloying of a pre-alloy powder produced by gas atomization followed by consolidation and mechanical processing, e.g. by means of hot extrusion [4]. An alternative consolidation method is based on field-assisted sintering, e.g. spark plasma sintering (SPS) [5]. The capability of SPS for scale up to the semi-industrial level in terms of sample volume was demonstrated [5,6]. Several consolidation methods including SPS tend to produce microstructures characterized by a pronounced bimodality of the grain size distribution [7–9].

The knowledge about the irradiation response, both under operation-relevant conditions and from a broader, more basic point of view, is still incomplete [10,11]. This is particularly true for fusion applications, where displacement (neutron) damage is combined with helium production [12]. A possible approach to emulate neutron irradiation damage and helium production is based on ion irradiations [10,13]. In spite of yet unsolved transferability issues, this kind of approach is needed because of the limited availability of proper irradiation facilities. It was shown before by way of nanoindentation experiments that displacement damage and He implantation give rise to synergistic irradiation effects on the hardness increase. In more detail, neither single-beam Fe-ion or He-ion irradiations nor sequential Fe-He or He-Fe irradiations are capable of reproducing the hardness increase observed after simultaneous (dual-beam) irradiations with Fe- and He-ions [14].

Nanoindentation has long been recognized as a tool to study ion-irradiation effects on the mechanical properties of nuclear materials [13,15–19]. This is because the covered depth ranges can be tuned via indentation load and/or ion energy to match one another. In the case of an Fe-ion-irradiated layer on an unirradiated Fe-based substrate, the elastic modulus is approximately equal for layer and substrate and independent of depth [20]. In such instances, it is straightforward to interpret the measured indentation hardness as the actual local hardness averaged over the volume of the indentation plastic zone [19,21–24], which reaches about 5 to 10 times deeper than the indentation contact depth [25]. This means that gradients of the displacement damage along the depth of the indentation plastic zone have to be considered. To avoid steep gradients, three- or multiple step irradiations were applied with the ion energy varied stepwise [17,18]. For the case of self-ion irradiations, this approach necessarily gives rise to the introduction of self-interstitial atoms throughout the irradiated depth range. As such excess self-interstitials are not formed upon neutron irradiation, they pose a transferability issue [26,27]. On the other hand, the interpretation of nanoindentation results as function of the local irradiation microstructure is not yet well understood for the case of steep damage gradients arising from single-beam irradiations.

In the present study, nanostructured ferritic ODS Fe-14%Cr-based alloys were fabricated by means of mechanical alloying of pre-alloy powders with 0.6 wt%  $Y_2O_3$  and consolidation by means of SPS. A Y-free control sample was also produced via the same route. After microstructure characterization of the as-fabricated alloys, selected samples were exposed to single-beam (Fe) and dual-beam (Fe+He) ion irradiations at room temperature (RT). The observed bimodality of the grain size distributions was

exploited to derive the irradiation-induced indentation-hardness increase for the fine-grained and coarser-grained regions individually. The aim of the study was to separate the effects of grain size and dispersed oxide nanoparticles on the irradiation-induced hardness increase. Comparisons of both dual-beam versus single-beam irradiations and ODS versus yttrium-free control allow the influence of oxide particles on helium management to be highlighted. Transferability issues to fusion-prototypic irradiation conditions are not envisaged except for the realistic value of the applied appm He/dpa ratio of approximately 10 [12].

## 2. Experiments

### 2.1 Materials and Samples

Two oxide-dispersion strengthened (ODS) Fe-14Cr-1W-0.4Ti materials (materials B and C) along with an yttrium-free control (material A) were selected from a broader set of produced materials. A gas atomized Fe-14Cr based pre-alloyed powder (Nanoval GmbH & Co. KG) was milled with and without 0.6 wt% of  $Y_2O_3$  powder (PCT Ltd., particle size  $\approx 30$  nm) in a Pulverisette P5 planetary ball mill in purified argon atmosphere with a ball-to-powder weight ratio of 10:1. The composition of the steel powder given in

Table 1 was intentionally chosen similar to the composition reported in [4,28] in order to facilitate cross comparison. The applied milling intensity was varied with respect to milling speed and milling time in order to achieve a set of alloys with different grain size and oxide particle size distributions. The milling parameters and  $Y_2O_3$  contents are given in Table 2. As there was no significant difference in the powder particle size distributions, no sieving was necessary to maintain comparable sintering behavior. The same sintering parameters were applied for all alloys. The consolidation was done under vacuum using an FCT-HP D 250/1 spark plasma sintering device (FCT Systeme GmbH) with a dwelling time of 10 min at a temperature of 1050 °C and a maximum pressure of 70 MPa applied after heating to 750 °C. Relative densities higher than 98% were achieved for all samples of diameter 30 mm and thickness of approximately 7 mm. Sample A was annealed under vacuum at 1350 °C for 7.5 h.

Table 1: Composition of the pre-alloyed steel powder. All values are given in wt%.

Fe	Cr	W	Ti	Mn	Si	Ni
<b>bal.</b>	14.10	0.99	0.32	0.34	0.18	0.17

Table 2:  $\text{Y}_2\text{O}_3$  content and milling parameters.

Sample	$\text{Y}_2\text{O}_3$ content (wt%)	Milling time (h)	Milling speed (rpm)
A	0.0	30	250
B	0.6	20	150
C	0.6	50	250

Small plates of size 10 mm x 10 mm x 1 mm were machined from the SPS samples using wire-cut EDM. All samples were wet ground with SiC paper and mechanically polished with diamond paste down to 1  $\mu\text{m}$  particle size before ion irradiation. As confirmed earlier by means of depth-resolved measurements of the S-parameter of positron annihilation spectroscopy, the thickness of the damage layer is less than 50 nm.

## 2.2 Microstructure characterization of the unirradiated materials

Electron backscatter diffraction (EBSD) was applied in order to evaluate the type of microstructure and the grain size for the whole set of samples. The Ultra 55 Plus FEG SEM (Carl Zeiss AG) was equipped with a HKL Nordlys F-type EBSD detector (Oxford Instruments plc). The measurements were carried out at 20 kV using a 120  $\mu\text{m}$  aperture at a working distance of 15 mm and a sample tilt of 70°. The Esprit software of Bruker was used for data post-processing. The minimum misorientation angle between neighboring grains was fixed at 5° for grain size determination.

The size distribution of oxide nanoparticles was derived by means of small-angle neutron scattering (SANS). The experiments were performed at the beamline D33 of ILL Grenoble using a neutron wavelength of 0.6 nm. Two sample-detector distances of 1.2 m and 12 m were realized to cover a wide range of the scattering vector  $Q$ . The samples with dimension 10 mm x 10 mm x 1 mm were placed in a magnetic field of 1.4 T in order to allow magnetic and nuclear scattering cross-sections to be separated. The SANS analysis and the results obtained for a broader set of samples including those of the present study were reported in [29]. Samples A, B and C of the present study correspond to A, D and F in [29].

The spatial distribution and composition of oxide nanoparticles were characterized by means of atom probe tomography (APT). The APT measurements were carried out using an IMAGO LEAP 3000X HR system at the Materials Department of the University of Oxford in laser mode and applying a

laser-pulse energy of 0.6 nJ. Reconstructions were made using the IVAS 3.0 software by Cameca. For more details see [30].

Transmission electron microscopy (TEM) was performed on a Talos F200X FEG-(S) TEM (FEI) operated at 200 keV. The spatial distribution of the oxide nanoparticles was characterized using bright field imaging. Samples were prepared by means of electropolishing in a Tenupol-5 in 5% perchloric acid in methanol at -60 °C employing a voltage of 23 V.

### 2.3 Ion irradiation

All ion irradiations with Fe- and He-ions (single-beam as well as dual-beam) were performed in the dual implantation chamber (DIC) at the Ion Beam Center (IBC) of HZDR, Dresden, Germany [31]. The DIC allows simultaneous implantation to be performed using two ion beams originating from a 500 kV implanter (He) and a 3 MV Tandetron accelerator (Fe) with an angle of incidence of 22.5°. The ion beams were synchronized and scanned over the area of the samples during the irradiation to guarantee a laterally uniform exposure over the whole set of samples. All irradiations were carried out at room temperature (RT).

Two irradiation modes were applied:

1. Single-beam implantation with Fe ions to nominally 10 dpa.
2. Simultaneous (dual-beam) implantation with He and Fe ions to 100 appm He and 10 dpa (He/dpa ratio approximately 10 appmHe/dpa).

Three-step irradiations with different ion energies were applied to produce a nearly homogeneous irradiated layer. The energies of Fe- and He-ions were chosen such that the maximum of the exposure profile of the Fe-ions and the maximum of the implantation profile of the He-ions coincide to ensure simultaneous implantation. The individual ion energies applied were 750 keV, 1.5 MeV and 3 MeV for Fe-ions and 50 keV, 150 keV, 350 keV for He-ions, respectively, which results in an irradiated layer of about 1 µm depth. The ion irradiations were performed in steps from lowest to highest ion energy. The ion irradiation parameters are given in

Table and 4. The exposure profile (in terms of dpa) is shown in Fig. 1. Geometric representations of the indenter and the indentation plastic zone (assumed to be a halfsphere), both for an indention depth of 100 nm, are superimposed to the plot.

The ion irradiation experiment was designed using the SRIM code (SRIM-2008.04) [32]. The exposure profile in terms of dpa were calculated based on Kinchin-Pease [33] using the quick calculation mode of SRIM with the lattice binding energy and the surface binding energy set to zero,

as suggested by Stoller [34]. The displacement energy was set to  $E_D = 40$  eV for a pure Fe-target according to ASTM-Standard E512 [35]. The contribution of He to the total exposure is less than 0.01 dpa.

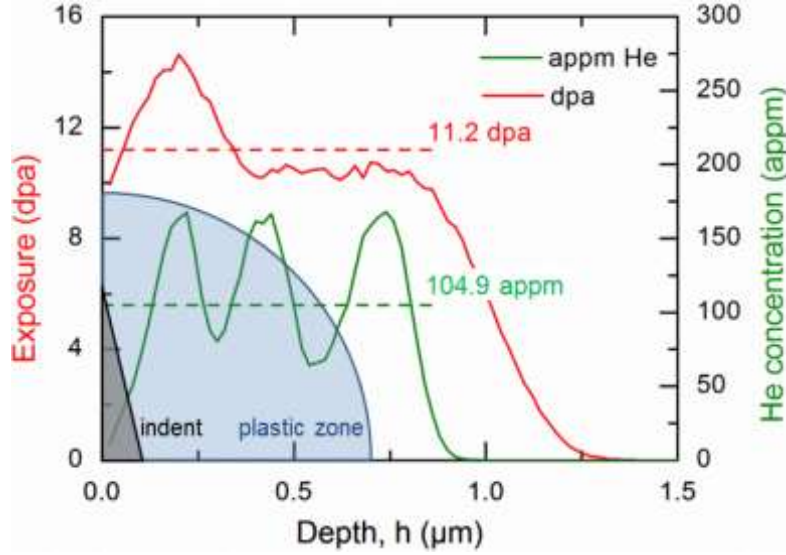


Fig. 1: Exposure (dpa) profile and He-concentration according to SRIM.

Table 3: Irradiation parameters for the three-step single-beam ion irradiations with Fe ions.

Step	Ion	Ion energy (keV)	Ion fluence ( $10^{15} \text{ cm}^{-2}$ )
(1)	$\text{Fe}^{2+}$	3000	9.6
(2)	$\text{Fe}^+$	1500	2.7
(3)	$\text{Fe}^+$	750	5.0

Table 4: Irradiation parameters for the multi-step dual-beam ion irradiations with Fe and He ions.

Step	Ion	Ion energy (keV)	Ion fluence ( $10^{15} \text{ cm}^{-2}$ )
(1)	$\text{He}^+$	350	0.34
(1)	$\text{Fe}^{2+}$	3000	9.6
(2)	$\text{He}^+$	150	0.27
(2)	$\text{Fe}^+$	1500	2.7

(3)	He <sup>+</sup>	50	0.20
(3)	Fe <sup>+</sup>	750	5.0

## 2.4 Nanoindentation

Nanoindentation testing was performed using the Universal Nanomechanical Tester (UNAT, Advanced Surface Mechanics GmbH, now part of the Zwick-Roell Group) equipped with a Berkovich indenter. The calibration of the indenter area function and the instrument stiffness was based on measurements on two reference materials (fused silica, sapphire) with known elastic modulus.

To obtain the indentation hardness as a function of depth from the loading curve, the Quasi Continuous Stiffness Measurement (QCSM) method [36] was applied. QCSM follows the same approach as the more familiar CSM (Continuous Stiffness Measurement) method [37], however the voltage of the piezoelectric resonator is not continuously overlaid with a sinusoidal oscillation during loading, but at discrete loading points. A maximum load of 50 mN was applied. The load cycle includes a holding segment of 60 s after partial unloading to 10% of the maximum load which is used to determine the thermal drift velocity.

Data processing included zero point correction and thermal drift correction. Zero point correction was performed manually. Thermal drift was accounted for by correcting the displacements as a function of time assuming the drift velocity to be constant over the whole measurements. In all cases, the total drift during the indentation test was at least an order of magnitude smaller than the measured total indentation depth. An average load displacement curve along with the standard deviation of load and displacement was calculated from the single corrected curves (for the number of curves see below). The data were analyzed according to a method developed by Doerner and Nix [38] and adapted to pyramidal indenters by Oliver and Pharr [39,40]. The indentation hardness at the selected reference depth of 100 nm (see Fig. 1) was obtained by interpolation taking into account the data points in the surrounding of the reference depth.

As will be shown below, materials B and C exhibit a pronounced bimodality of the grain size distribution. This observation was exploited to obtain the indentation hardness for the fine-grained and coarse-grained areas separately. To this end, arrays of indentations covering fine-grained and coarse-grained regions of the same samples were defined. By superimposing the arrays with EBSD images, the individual indentations were retrospectively assigned either to the fine-grained area, or to the coarse-grained area, or classified as unclear borderline cases. For the former two cases, at least 20 indentation tests each were collected.



### 3. Results

#### 3.1 Characterization of the unirradiated materials

EBSD inverse pole figure maps of the microstructure of the materials A, B and C are shown in Fig. 2. Material A exhibits a homogeneous microstructure in terms of grain size. In contrast, materials B and C show bimodal grain size distributions with areas of larger grains (size range 1 to 10  $\mu\text{m}$ ) and ultrafine grains (size range 0.1 to 1  $\mu\text{m}$ ). The experimentally estimated values of the mean grain size for material A and the coarse- and fine-grained regions of materials B and C are given in Table 5.

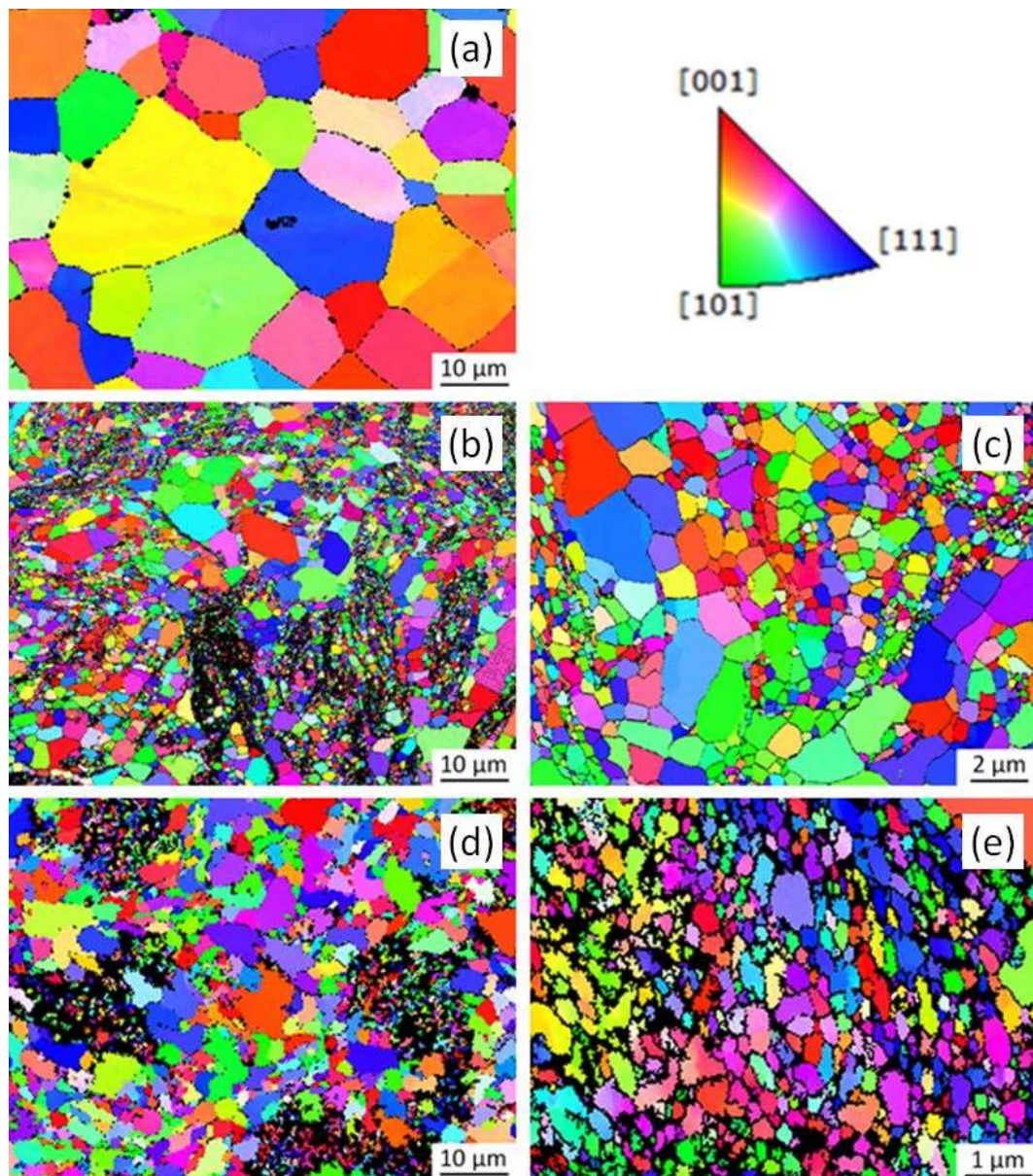


Fig. 2: EBSD inverse pole figure maps of the Y-free reference sample A (a), the ODS sample B (b), (c), and the ODS sample C (d), (e). The IPF map in Fig. 2 (e) was taken in the fine-grained area.

Table 5: Mean grain size  $d$  in coarse- and fine-grained areas.

Sample	$d$ (coarse) ( $\mu\text{m}$ )	$d$ (fine) ( $\mu\text{m}$ )
A	6.79	-
B	1.15	0.32
C	1.51	0.19

The projections of the 3D atom probe reconstructions rotated around the z-axis in Fig. 3 reveal oxide particles with a size below 10 nm in sample B (powder milled for 20 h, 150 rpm), which are aligned on a plane with extended particle-free zones around. For sample C, which was produced with a higher milling time and speed (50 h, 250 rpm) applied, the detected Y-Ti containing oxide particles are homogeneously distributed within the analyzed volume. As the volumes probed by APT are comparably small, TEM was applied in order to verify the gained information.

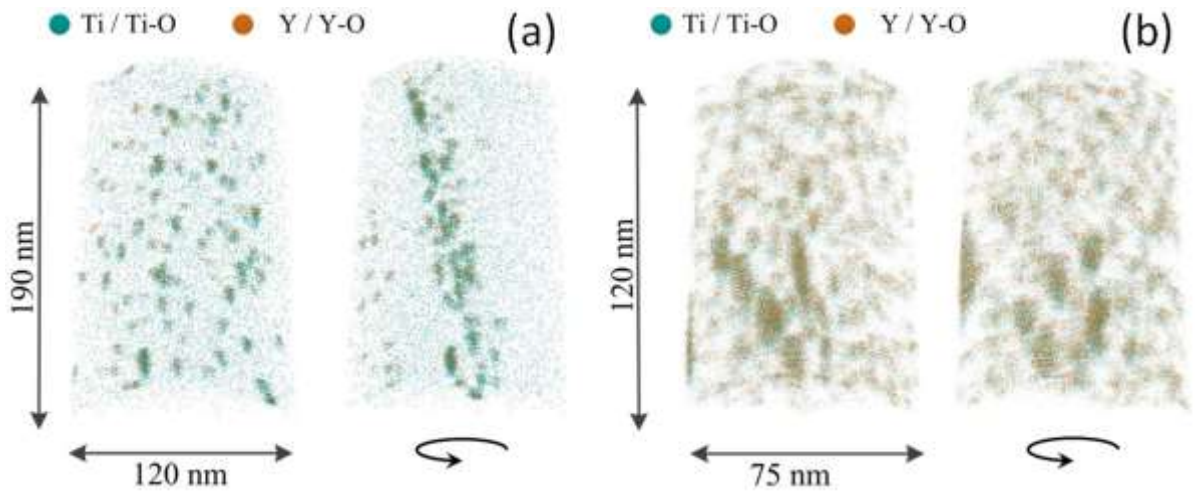


Fig. 3: Projected 3D atom maps obtained from APT displaying the spatial distribution of Y-Ti oxide particles in materials B (a) and C (b). The maps displayed in (a) are rotated projections of the same 3D map. The same is applicable for the maps displayed in (b).

TEM images of samples B and C are provided in Fig. 4. After 20 h of milling at 150 rpm (sample B, Fig. 4 (a)), large oxide particles with a size up to 100 nm are present along with the nm-size oxide particles detected by means of APT. The TEM micrograph was intentionally taken in overfocus in order to better visualize the smallest oxide particles. The occurrence of extended particle-free zones was confirmed. For sample C (Fig. 4 (b)), the homogeneous distribution of nm-size oxide particles without particle-free zones was verified. It is interesting to note that no obvious correlation between fine- or coarse-grained areas and particle-free zones was found.

In contrast to APT and TEM, which provide a local picture of the microstructure along with the spatial distribution of nanoparticles, SANS allows macroscopically representative and statistically reliable averages of the nanoparticles to be derived. The total number density and volume fraction of oxide nanoparticles in the size range 0.5-15 nm (radius) are summarized in Table 6. It is important to note that the large oxide particles present in B (see Fig. 4) do not contribute to these values, as their size exceeds the particle size range investigated with SANS. The complete set of results including other samples was reported in [30]. The dominant smaller fraction of nanoparticles were concluded to be  $\text{Y}_2\text{Ti}_2\text{O}_7$  and/or  $\text{Y}_2\text{TiO}_5$  for both sample B and C, while sample A contains a smaller amount of yttrium-free oxide nanoparticles.

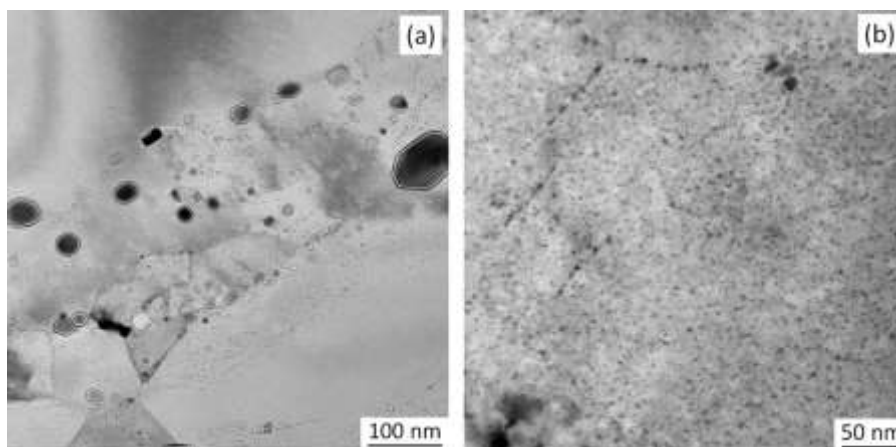


Fig. 4: TEM images of ODS materials B (a) and C (b) displaying the presence of non-uniformly distributed oxide particles with a size up to 100 nm in B and a uniform distribution of nm-size oxide particles in C.

Table 6: Total number density  $N$  and volume fraction  $f$  of particles in the size range 0.5 - 15 nm, obtained from SANS measurements.

<b>Sample</b>	<b><math>N</math></b>	<b><math>f</math></b>
	<b>(<math>10^{16} \text{ cm}^{-3}</math>)</b>	<b>(vol%)</b>
<b>A</b>	$8 \pm 3$	$0.17 \pm 0.01$
<b>B</b>	$25 \pm 20$	$0.46 \pm 0.04$
<b>C</b>	$71 \pm 34$	$1.16 \pm 0.06$

### 3.2 Irradiation response

The measured indentation hardness  $H_i$  vs. contact depth  $h_c$  of the selected samples in the unirradiated as well as in single-beam (SB) and dual-beam (DB) irradiated conditions is plotted in Fig. 5. All indentation hardness values  $H_i$  interpolated from the curves in Fig. 5 for the selected reference contact depth of 100 nm are summarized in Table 7. The contribution arising from the unirradiated substrate is negligible for this reference depth. The indentation size effect (ISE) is assumed to be similar for the irradiated and unirradiated conditions. As the differences  $\Delta H_i$  of the indentation hardness between the irradiated conditions and the unirradiated controls are evaluated, the ISE contribution can be neglected in the discussion. In Fig. 5, Table 7 and what follows, the coarse-grained (subscript c) and fine-grained (subscript f) areas of materials B and C are treated such as if they belonged to individual samples.



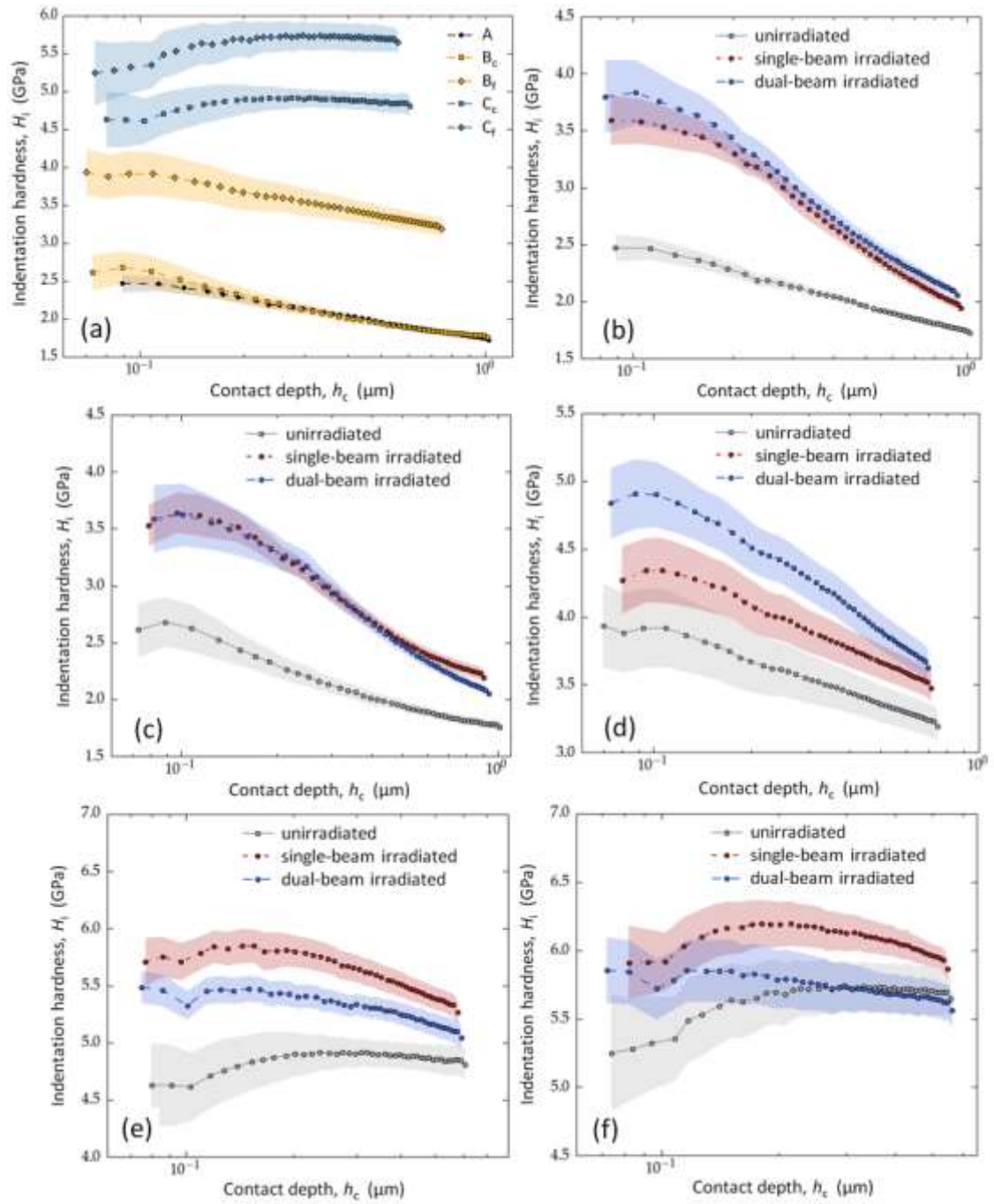


Fig. 1: Indentation hardness vs. contact depth for the unirradiated conditions of all materials (a) as well as the unirradiated, single-beam irradiated and dual-beam irradiated conditions of material A (b), the coarse-grained area of material B (c), the fine-grained area of B (d), the coarse-grained area of C (e), and the fine-grained area of C (f).

Table 7: Indentation hardness of unirradiated, single-beam (SB) and dual-beam (DB) irradiated samples and the resulting irradiation-induced hardness increase.

Sample	Unirradiated $H_i$ (GPa)	SB $H_i$ (GPa)	SB $\Delta H_i$ (GPa)	DB $H_i$ (GPa)	DB $\Delta H_i$ (GPa)
A	$2.47 \pm 0.12$	$3.58 \pm 0.07$	$1.11 \pm 0.14$	$3.80 \pm 0.20$	$1.33 \pm 0.23$
B <sub>c</sub>	$2.64 \pm 0.11$	$3.64 \pm 0.15$	$1.00 \pm 0.19$	$3.59 \pm 0.21$	$0.95 \pm 0.24$
B <sub>f</sub>	$3.92 \pm 0.13$	$4.34 \pm 0.08$	$0.42 \pm 0.15$	$4.89 \pm 0.12$	$0.97 \pm 0.18$
C <sub>c</sub>	$4.64 \pm 0.18$	$5.79 \pm 0.15$	$1.14 \pm 0.23$	$5.46 \pm 0.08$	$0.82 \pm 0.19$
C <sub>f</sub>	$5.35 \pm 0.29$	$5.97 \pm 0.12$	$0.61 \pm 0.31$	$5.85 \pm 0.09$	$0.50 \pm 0.30$

The irradiation-induced hardening due to single-beam (Fe) and dual-beam (Fe+He) ion irradiation of the investigated samples is summarized in Fig. 6 (a) and (b), respectively. The hardness increase caused by single-beam and dual-beam irradiations is compared in Fig. 6(c) for materials A and C. Material B is excluded from this comparison because of the uncertainties introduced by the observed heterogeneous distribution of oxide nanoparticles. It is important to note that the errors in Fig. 6(c) are smaller than the respective errors in (a) and (b), because the same unirradiated control was subtracted from the hardness values observed after single-beam and dual-beam irradiations, meaning that the error of the control hardness drops out for the comparison between DB and SB.

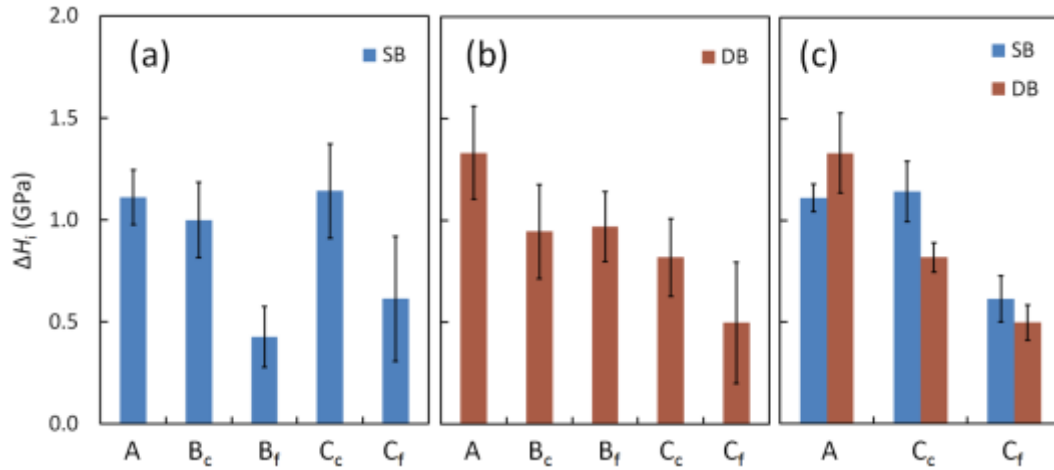


Fig. 2: Irradiation-induced hardening of the studied materials due to single-beam (SB) ion irradiation (a) and dual-beam (DB) ion irradiation (b), comparison of SB and DB irradiations (c).

#### 4. Discussion

It is necessary to work out some microstructural features of particular importance for the irradiation behavior in more detail.

We have observed a pronounced bimodality of the grain size distributions for materials B and C. This is in agreement with findings reported for the same kind of material also fabricated by way of mechanical alloying and consolidation by SPS [8], which leads us to assume that bimodality is a characteristic feature for this fabrication route. The origin of the bimodality was studied in [41] in terms of abnormal grain growth. These authors found that precipitation is not the major cause of both abnormal growth and the resulting bimodality of the grain size distribution. Instead, abnormal growth is a consequence of the initial heterogeneous spatial distribution of the stored energy due to high-energy milling. With respect to the present study, we conclude that bimodal grain size distributions can be (material B), but are not necessarily (material C), associated with particle-free zones. In contrast, the dislocation densities associated with the fine-grained and coarse-grained areas are necessarily different. This means that the higher sink strength (for irradiation-induced point defects, see below) associated with the fine-grained areas is additionally magnified via the sink strength contribution arising from the higher dislocation density in the fine-grained areas.

In addition to the characteristics of the oxide particle distributions summarized in Table 6, it is also important to consider the type of particles and particle-matrix interfaces. Information on that was derived from the ratio of magnetic and nuclear scattering of SANS (A-ratio) [29] and from an APT study [30]. For material C (material F in [29,30]), the smallest particles of radii between 0.5 and 3 nm were concluded to dominate in terms of both number density and volume fraction and to be of type  $Y_2Ti_2O_7$  or  $Y_2TiO_5$ . Particles of both types coexist. After some debate in the literature, the dominance of types  $Y_2Ti_2O_7$  and  $Y_2TiO_5$  is now generally accepted [3]. In this respect, it is important to note that the A-ratio of SANS represents an average over a macroscopic volume of the order of  $50 \text{ mm}^3$ .  $Y_2Ti_2O_7$ -type particles were reported to be coherent at the entire interface with a cube-on-cube orientation relationship [42].

The further discussion is based on the findings on hardening summarized in Fig. 6 in conjunction with the initial microstructures. We shall begin with the single-beam irradiations, Fig. 6(a). Samples A, B<sub>c</sub> and C<sub>c</sub> (group 1) exhibit similar irradiation hardening. Samples B<sub>f</sub> and C<sub>f</sub> (group 2) exhibit significantly lower irradiation hardening. On the one hand, the significant difference between groups 1 and 2 is related to the grain size: Grain sizes well below  $1 \text{ }\mu\text{m}$  give rise to less irradiation hardening than grain sizes in excess of  $1 \text{ }\mu\text{m}$ . As rationalized above, the grain size effect on hardening is potentially associated with an effect of the dislocation density. On the other hand, the approximate agreement (i.e. insignificant differences) of irradiation hardening inside each of the groups 1 and 2 indicates that irradiation hardening does not depend on the characteristics of the oxide nanoparticles.

The situation is essentially different for dual-beam irradiations, Fig. 6(b). Grain size/dislocation density still seems to make a difference, although this is not as clear as for the single-beam case. But contrary to single beam, the characteristics of the oxide nanoparticles in terms of number density or volume fraction do play a significant role. There is a clear trend of irradiation hardening to decrease at increasing number density. Obviously, the role of He is crucial for this finding. Indeed, as shown in Fig. 6(c), the implantation of He atoms (simultaneously with the introduction of displacement damage) gives rise to an increase of irradiation hardening for material A and a decrease of irradiation hardening for material C.

The findings related to irradiation hardening as observed under the present conditions are summarized as follows:

- (1) Significant irradiation-induced increases of hardness are observed for each material and each irradiation condition of this study.
- (2) Smaller grain size (and higher dislocation density) gives rise to less hardening for single-beam irradiations.
- (3) Oxide nanoparticles do not alter hardening for single-beam irradiations.
- (4) Smaller grain size (and higher dislocation density) tends to reduce hardening for dual-beam irradiations
- (5) Higher number densities of oxide nanoparticles give rise to less hardening for dual-beam irradiations.
- (6) DB irradiation gives rise to more hardening than SB irradiation for material A.
- (7) DB irradiation gives rise to less hardening than SB irradiation for material C.

It is important to emphasize that the experimental characterization of the families of irradiation-induced nanofeatures and the identification of their respective roles in irradiation hardening in the present materials are beyond the scope of this study. However, it is still important to see, if and how reported insight into both the formation of defects and the role of microstructural features is consistent with our findings.

To this end, it is important to recap two peculiarities of the present irradiation experiments, namely (a) the introduction of excess self-interstitials throughout the depth range relevant for nanoindentation testing, see introduction, and (b) irradiations performed at RT. Under thermal conditions at RT, interstitials (migration energy  $E_{mi} = 0.3$  eV [43]) are mobile and can quickly reach any kind of available and attractive sinks. In contrast, vacancies (migration energy  $E_{mv} = 1.3$  eV [43]) are practically immobile. He diffusion via an interstitial mechanism (migration energy  $E_{mHe(int)} = 0.06$  eV [44]) gives rise to extremely high mobility. However, as soon as a He atom finds a vacancy, it becomes strongly bound to it (binding energy  $E_{bHe(int)-V} = 2.3$  eV [44]) and the He-V complex is practically immobile at RT [45]. The mean free diffusional path of a species given by  $x = 2\sqrt{(Dt)}$ ,



where  $D$  and  $t$  are diffusivity and a reference time, respectively, has to be compared with characteristic lengths of the microstructure such as grain size and interparticle spacing.

With this background, we are prepared to address findings (1) to (7) listed above:

(1) Irradiation hardening is assumed to be mainly due to dislocation loops in the SB case and additionally to He bubbles in the DB case. Many studies (e.g. [46,47] reported evidence for loop formation under irradiation at RT. Substantial hardening due to nanovoids can be excluded because of the low mobility of vacancies and small vacancy clusters as well as the excess of interstitials. The excess interstitials were also reported to suppress the formation of Cr-rich  $\alpha'$ -phase particles [27]. Moreover, it is reasonable to assume that the oxide nanoparticles are stable under the present irradiation conditions [48,49] and do not significantly alter their intrinsic hardening contribution. For the DB case, He bubbles formed in the matrix are expected to contribute to irradiation hardening, while bubbles associated with grain boundaries (GBs) or particle-matrix interfaces can be assumed to be of minor significance, because GBs and particles contribute to hardening anyway.

(2) The smaller the grain size the higher the fraction of interstitials that can be trapped in GBs [11,50]. These interstitials can lose their identity or can be reemitted to recombine with matrix vacancies according to the mechanism proposed in [51]. In any case, the smaller the grain size, the more interstitials are removed from the system. The removed interstitials are no longer available for loop formation and hardening. The same reasoning can be put forth for dislocations, the density of which is higher for the fine-grained regions.

(3) Obviously, the particle-matrix interface is incapable of efficiently trapping interstitials, the most stable configuration of which is the  $\langle 110 \rangle$  dumbbell. As incoherent boundaries generally can trap interstitials, this must be a consequence of the coherency of the interfaces.

(4) See (2). Additionally, GBs are known to be efficient traps for He atoms. On the one hand, these He atoms are removed from the matrix and, therefore, not available for the formation of He bubbles in the matrix. On the other hand, He atoms or bubbles at the GB are expected to alter the hardening contribution, posed by the GBs anyway, only marginally.

(5) Obviously, the coherent particle-matrix interfaces can efficiently trap He atoms. This idea was put forth earlier and has been rationalized recently [52]. On the one hand, these He atoms are removed from the matrix and, therefore, not available for the formation of He bubbles in the matrix. On the other hand, He atoms or bubbles associated with oxide nanoparticles are expected to alter the hardening contribution, posed by the particles anyway, only marginally (see also (4) above).

(6) As He implantation is added to the self-ion irradiation, higher hardening is what one would naturally expect. The extra hardening may be due to He bubbles in the matrix, in particular in cases, in which He is not efficiently trapped in GBs or particle-matrix interfaces. This is the case for material A.

(7) This result is counterintuitive and no rationalization was found in the literature. Apparently, He atoms or bubbles trapped at coherent interfaces give rise to additional trapping of self-interstitial atoms.

## 5. Conclusions

Two ODS nanoferritic Fe-14Cr-based alloys and a Y-free reference alloy produced via mechanical alloying and consolidation by spark plasma sintering were characterized by means of EBSD, SANS, APT and TEM and exposed to single-beam (Fe) and dual-beam (Fe + He) ion irradiations at RT. The microstructure characterization of the ODS alloys revealed bimodal grain-size distributions and dispersions of mainly coherent oxide nanoparticles of types  $\text{Y}_2\text{Ti}_2\text{O}_7$  and  $\text{Y}_2\text{TiO}_5$  in the size range from 0.5 to 3 nm (radius). Nanoindentation testing in the fine-grained and coarse-grained regions allowed irradiation hardening to be considered as a function of grain size.

We have found that the irradiation-induced hardness increase depends only on grain size for single-beam irradiations, but on both grain size and particle number density for dual-beam irradiations. This sheds a light on the role of GBs and coherent particle-matrix interfaces in the evolution of irradiation-induced defect clusters and helium management. In particular, the coherent interfaces seem to trap He but not self-interstitials (in the absence of He).

While most of the observations were found to be consistent with existing insight on defect formation and defect-interface interaction, reduced hardening due to DB irradiation as compared to SB irradiation is counterintuitive and requires further consideration.

## Acknowledgement

This work received partial funding by the European Commission within the MATTER project (Grant Agreement No. 269706) and MATISSE project (Grant Agreement No. 604862). EBSD was performed at the Leibniz Institute for Solid State and Materials Research Dresden. Many thanks to Horst Wendrock for his help. The transmission electron microscope Talos was funded by the German Federal Ministry of Education and Research (BMBF) (grant no. 03SF0451) in the framework of the Helmholtz Energy Materials Characterization Platform (HEMCP). The possibility to perform APT during a stay of I.H. at the Department of Materials at the University of Oxford is also gratefully acknowledged. The ion irradiations were carried out at IBC at the Helmholtz-Zentrum Dresden-Rossendorf.

## References

- [1] P. Yvon, F. Carré, Structural materials challenges for advanced reactor systems, *J. Nucl. Mater.* 385 (2009) 217–222. doi:10.1016/j.jnucmat.2008.11.026.
- [2] A. Kimura, W. Han, H. Je, K. Yabuuchi, R. Kasada, Oxide Dispersion Strengthened Steels for Advanced Blanket Systems, *Plasma Fusion Res.* 11 (2016) 2505090–2505090. doi:10.1585/pfr.11.2505090.
- [3] G.R. Odette, On the status and prospects for nanostructured ferritic alloys for nuclear fission and fusion application with emphasis on the underlying science, *Scr. Mater.* 143 (2018) 142–148. doi:10.1016/j.scriptamat.2017.06.021.
- [4] P. Dubuisson, Y. de Carlan, V. Garat, M. Blat, ODS Ferritic/martensitic alloys for Sodium Fast Reactor fuel pin cladding, *J. Nucl. Mater.* 428 (2012) 6–12. doi:10.1016/j.jnucmat.2011.10.037.
- [5] P. Franke, C. Heintze, F. Bergner, T. Weissgaerber, Mechanical Properties of Spark Plasma Sintered Fe-Cr Compacts Strengthened by Nanodispersed Yttria Particles, *Mater. Test.-Mater. Compon. Technol. Appl.* 52 (2010) 133–138.
- [6] X. Boulnat, D. Fabrègue, M. Perez, S. Urvoy, D. Hamon, Y. de Carlan, Assessment of consolidation of oxide dispersion strengthened ferritic steels by spark plasma sintering: from laboratory scale to industrial products, *Powder Metall.* 57 (2014) 204–211. doi:10.1179/1743290114Y.0000000091.
- [7] Z. Dapeng, L. Yong, L. Feng, W. Yuren, Z. Liuji, D. Yuhai, ODS ferritic steel engineered with bimodal grain size for high strength and ductility, *Mater. Lett.* 65 (2011) 1672–1674. doi:10.1016/j.matlet.2011.02.064.
- [8] X. Boulnat, M. Perez, D. Fabregue, T. Douillard, M.-H. Mathon, Y. de Carlan, Microstructure Evolution in Nano-reinforced Ferritic Steel Processed By Mechanical Alloying and Spark Plasma Sintering, *Metall. Mater. Trans. A.* 45 (2014) 1485–1497. doi:10.1007/s11661-013-2107-y.
- [9] I. Hilger, F. Bergner, T. Weissgaerber, Bimodal Grain Size Distribution of Nanostructured Ferritic ODS Fe-Cr Alloys, *J. Am. Ceram. Soc.* 98 (2015) 3576–3581. doi:10.1111/jace.13833.
- [10] T. Yamamoto, Y. Wu, G. Robert Odette, K. Yabuuchi, S. Kondo, A. Kimura, A dual ion irradiation study of helium–dpa interactions on cavity evolution in tempered martensitic steels and nanostructured ferritic alloys, *J. Nucl. Mater.* 449 (2014) 190–199. doi:10.1016/j.jnucmat.2014.01.040.
- [11] I.J. Beyerlein, M.J. Demkowicz, A. Misra, B.P. Uberuaga, Defect-interface interactions, *Prog. Mater. Sci.* 74 (2015) 125–210. doi:10.1016/j.pmatsci.2015.02.001.
- [12] J. Knaster, A. Moeslang, T. Muroga, Materials research for fusion, *Nat. Phys.* (2016) 424–434. doi:10.1038/nphys3735.

- [13] Y. Katoh, M. Ando, A. Kohyama, Radiation and helium effects on microstructures, nano-indentation properties and deformation behavior in ferrous alloys, *J. Nucl. Mater.* 323 (2003) 251–262. doi:10.1016/j.jnucmat.2003.08.007.
- [14] C. Heintze, F. Bergner, M. Hernández-Mayoral, R. Kögler, G. Müller, A. Ulbricht, Irradiation hardening of Fe–9Cr-based alloys and ODS Eurofer: Effect of helium implantation and iron-ion irradiation at 300 °C including sequence effects, *J. Nucl. Mater.* 470 (2016) 258–267. doi:10.1016/j.jnucmat.2015.12.041.
- [15] P.M. Rice, R.E. Stoller, The effect of solutes on defect distributions and hardening in ion-irradiated model ferritic alloys, *J. Nucl. Mater.* 244 (1997) 219–226.
- [16] F.M. Halliday, D.E. Armstrong, J.D. Murphy, S.G. Roberts, Nanoindentation and micromechanical testing of iron-chromium alloys implanted with iron ions, in: *Adv. Mater. Res., Trans Tech Publ*, 2009: pp. 304–307.
- [17] C. Heintze, C. Recknagel, F. Bergner, M. Hernandez-Mayoral, A. Kolitsch, Ion-irradiation-induced damage of steels characterized by means of nanoindentation, *Nucl. Instrum. METHODS Phys. Res. Sect. B-BEAM Interact. Mater. At.* 267 (2009) 1505–1508. doi:10.1016/j.nimb.2009.01.122.
- [18] P. Hosemann, C. Vieh, R.R. Greco, S. Kabra, J.A. Valdez, M.J. Cappiello, S.A. Maloy, Nanoindentation on ion irradiated steels, *J. Nucl. Mater.* 389 (2009) 239–247. doi:10.1016/j.jnucmat.2009.02.026.
- [19] C. Shin, H. Jin, M.-W. Kim, Evaluation of the depth-dependent yield strength of a nanoindented ion-irradiated Fe–Cr model alloy by using a finite element modeling, *J. Nucl. Mater.* 392 (2009) 476–481. doi:10.1016/j.jnucmat.2009.04.011.
- [20] C. Heintze, F. Bergner, S. Akhmadaliev, E. Altstadt, Ion irradiation combined with nanoindentation as a screening test procedure for irradiation hardening, *J. Nucl. Mater.* 472 (2016) 196–205. doi:10.1016/j.jnucmat.2015.07.023.
- [21] A. Kareer, A. Prasitthipayong, D. Krumwiede, D.M. Collins, P. Hosemann, S.G. Roberts, An analytical method to extract irradiation hardening from nanoindentation hardness-depth curves, *J. Nucl. Mater.* 498 (2018) 274–281. doi:10.1016/j.jnucmat.2017.10.049.
- [22] M. Saleh, Z. Zaidi, M. Ionescu, C. Hurt, K. Short, J. Daniels, P. Munroe, L. Edwards, D. Bhattacharyya, Relationship between damage and hardness profiles in ion irradiated SS316 using nanoindentation – Experiments and modelling, *Int. J. Plast.* 86 (2016) 151–169. doi:10.1016/j.ijplas.2016.08.006.
- [23] F. Röder, C. Heintze, S. Pecko, S. Akhmadaliev, F. Bergner, A. Ulbricht, E. Altstadt, Nanoindentation of ion-irradiated reactor pressure vessel steels – model-based interpretation and comparison with neutron irradiation, *Philos. Mag.* 98 (2018) 911–933. doi:10.1080/14786435.2018.1425007.

- [24] A. Ruiz-Moreno, P. Hähner, Indentation size effects of ferritic/martensitic steels: A comparative experimental and modelling study, *Mater. Des.* 145 (2018) 168–180.  
doi:10.1016/j.matdes.2018.02.064.
- [25] C.K. Dolph, D.J. da Silva, M.J. Swenson, J.P. Wharry, Plastic zone size for nanoindentation of irradiated Fe–9%Cr ODS, *J. Nucl. Mater.* 481 (2016) 33–45. doi:10.1016/j.jnucmat.2016.08.033.
- [26] S.J. Zinkle, L.L. Snead, Opportunities and limitations for ion beams in radiation effects studies: Bridging critical gaps between charged particle and neutron irradiations, *Scr. Mater.* 143 (2018) 154–160. doi:10.1016/j.scriptamat.2017.06.041.
- [27] O. Tissot, C. Pareige, E. Meslin, B. Décamps, J. Henry, Influence of injected interstitials on  $\alpha'$  precipitation in Fe–Cr alloys under self-ion irradiation, *Mater. Res. Lett.* 5 (2017) 117–123.  
doi:10.1080/21663831.2016.1230896.
- [28] I. Hilger, X. Boulnat, J. Hoffmann, C. Testani, F. Bergner, Y. De Carlan, F. Ferraro, A. Ulbricht, Fabrication and characterization of oxide dispersion strengthened (ODS) 14Cr steels consolidated by means of hot isostatic pressing, hot extrusion and spark plasma sintering, *J. Nucl. Mater.* 472 (2016) 206–214. doi:10.1016/j.jnucmat.2015.09.036.
- [29] I. Hilger, F. Bergner, A. Ulbricht, A. Wagner, T. Weißgärber, B. Kieback, C. Heintze, C.D. Dewhurst, Investigation of spark plasma sintered oxide-dispersion strengthened steels by means of small-angle neutron scattering, *J. Alloys Compd.* 685 (2016) 927–935.  
doi:10.1016/j.jallcom.2016.06.238.
- [30] Isabell Hilger, Influence of microstructure features on the irradiation behaviour of ODS Fe-14Cr alloys, PhD Thesis, Technische Universität Dresden, 2017.
- [31] J.R. Kaschny, R. Kögler, H. Tyrroff, W. Bürger, F. Eichhorn, A. Mücklich, C. Serre, W. Skorupa, Facility for simultaneous dual-beam ion implantation, *Nucl. Instrum. Methods Phys. Res. Sect. Accel. Spectrometers Detect. Assoc. Equip.* 551 (2005) 200–207.  
doi:10.1016/j.nima.2005.06.046.
- [32] J.F. Ziegler, *The Stopping and Range of Ions in Matter*, Elsevier Science & Technology Books, 1985.
- [33] P. Sigmund, A note on integral equations of the Kinchin-Pease type, *Radiat. Eff.* 1 (1969) 15–18.
- [34] R.E. Stoller, M.B. Toloczko, G.S. Was, A.G. Certain, S. Dwaraknath, F.A. Garner, On the use of SRIM for computing radiation damage exposure, *Nucl. Instrum. Methods Phys. Res. Sect. B Beam Interact. Mater. At.* 310 (2013) 75–80. doi:10.1016/j.nimb.2013.05.008.
- [35] ASTM Standard E 521, Standard Practice for Neutron Radiation Damage Simulation by Charged-Particle Irradiation, ASTM International, West Conshohocken, PA, 2003., 1996.
- [36] Asmec GmbH, A new method for depth-resolved measurements of hardness and modulus, (n.d.).

- [37] X. Li, B. Bhushan, A review of nanoindentation continuous stiffness measurement technique and its applications, *Mater. Charact.* 48 (2002) 11–36.
- [38] M.F. Doerner, W.D. Nix, A method for interpreting the data from depth-sensing indentation instruments, *J Mater Res.* (1986) 601–609.
- [39] W.C. Oliver, G.M. Pharr, An improved technique for determining hardness and elastic modulus using load and displacement sensing indentation experiments, *J. Mater. Res.* 7 (1992) 1564–1583.
- [40] W.C. Oliver, G.M. Pharr, Measurement of hardness and elastic modulus by instrumented indentation: Advances in understanding and refinements to methodology, *J. Mater. Res.* 19 (2004) 3–20.
- [41] N. Sallel, X. Boulmat, A. Borbély, J.L. Béchade, D. Fabrègue, M. Perez, Y. de Carlan, L. Henet, C. Mocuta, D. Thiaudière, Y. Bréchet, In situ characterization of microstructural instabilities: Recovery, recrystallization and abnormal growth in nanoreinforced steel powder, *Acta Mater.* 87 (2015) 377–389. doi:10.1016/j.actamat.2014.11.051.
- [42] J. Ribis, Y. de Carlan, Interfacial strained structure and orientation relationships of the nanosized oxide particles deduced from elasticity-driven morphology in oxide dispersion strengthened materials, *Acta Mater.* 60 (2012) 238–252. doi:10.1016/j.actamat.2011.09.042.
- [43] A.H. Duparc, C. Moingeon, N. Smetniansky-de-Grande, A. Barbu, Microstructure modelling of ferritic alloys under high flux 1 MeV electron irradiations, *J. Nucl. Mater.* 302 (2002) 143–155.
- [44] C.-C. Fu, F. Willaime, *Ab initio* study of helium in  $\alpha$  – Fe : Dissolution, migration, and clustering with vacancies, *Phys. Rev. B.* 72 (2005). doi:10.1103/PhysRevB.72.064117.
- [45] C.J. Ortiz, M.J. Caturla, C.C. Fu, F. Willaime, He diffusion in irradiated  $\alpha$  – Fe : An *ab-initio* -based rate theory model, *Phys. Rev. B.* 75 (2007). doi:10.1103/PhysRevB.75.100102.
- [46] M. Hernández-Mayoral, Z. Yao, M.L. Jenkins, M.A. Kirk, Heavy-ion irradiations of Fe and Fe–Cr model alloys Part 2: Damage evolution in thin-foils at higher doses, *Philos. Mag.* 88 (2008) 2881–2897. doi:10.1080/14786430802380477.
- [47] V. de Castro, S. Lozano-Perez, M. Briceno, P. Trocellier, S.G. Roberts, R. Pareja, Effects of single- and simultaneous triple-ion-beam irradiation on an oxide dispersion-strengthened Fe12Cr steel, *J. Mater. Sci.* 50 (2015) 2306–2317. doi:10.1007/s10853-014-8794-y.
- [48] J.P. Wharry, M.J. Swenson, K.H. Yano, A review of the irradiation evolution of dispersed oxide nanoparticles in the b.c.c. Fe-Cr system: Current understanding and future directions, *J. Nucl. Mater.* 486 (2017) 11–20. doi:10.1016/j.jnucmat.2017.01.009.
- [49] V. de Castro, M. Briceno, S. Lozano-Perez, P. Trocellier, S.G. Roberts, R. Pareja, TEM characterization of simultaneous triple ion implanted ODS Fe12Cr, *J. Nucl. Mater.* 455 (2014) 157–161. doi:10.1016/j.jnucmat.2014.05.064.

- [50] B.N. Singh, Effect of grain size on void formation during high-energy electron irradiation of austenitic stainless steel, *Philos. Mag. J. Theor. Exp. Appl. Phys.* 29 (1974) 25–42.  
doi:10.1080/14786437408213551.
- [51] X.-M. Bai, A.F. Voter, R.G. Hoagland, M. Nastasi, B.P. Uberuaga, Efficient annealing of radiation damage near grain boundaries via interstitial emission, *Science*. 327 (2010) 1631–1634.
- [52] L. Yang, Y. Jiang, Y. Wu, G.R. Odette, Z. Zhou, Z. Lu, The ferrite/oxide interface and helium management in nano-structured ferritic alloys from the first principles, *Acta Mater.* 103 (2016) 474–482. doi:10.1016/j.actamat.2015.10.031.